

Modelling of an afterglow plasma in air produced by a pulsed discharge

This article has been downloaded from IOPscience. Please scroll down to see the full text article.

2010 Plasma Sources Sci. Technol. 19 055001

(<http://iopscience.iop.org/0963-0252/19/5/055001>)

View [the table of contents for this issue](#), or go to the [journal homepage](#) for more

Download details:

IP Address: 193.136.137.12

The article was downloaded on 17/11/2010 at 09:57

Please note that [terms and conditions apply](#).

Modelling of an afterglow plasma in air produced by a pulsed discharge

C D Pintassilgo^{1,2}, V Guerra¹, O Guaitella³ and A Rousseau³

¹ Instituto de Plasmas e Fusão Nuclear, Instituto Superior Técnico, 1049-001 Lisboa, Portugal

² Departamento de Engenharia Física, Faculdade de Engenharia, Universidade do Porto, R. Dr Roberto Frias, 4200-465 Porto, Portugal

³ Laboratoire de Physique des Plasmas, Ecole Polytechnique, CNRS, 91128, Palaiseau Cedex, France

E-mail: cdp@fe.up.pt

Received 22 December 2009, in final form 4 June 2010

Published 20 September 2010

Online at stacks.iop.org/PSST/19/055001

Abstract

A kinetic model is developed to study the afterglow plasma of a pulsed discharge in air. This model includes a detailed analysis of the temporal evolution of heavy species during the pulse, followed by their relaxation in the afterglow. The predicted results are compared with two experimental sets performed in the time afterglow of a pulsed discharge in N₂–20%O₂ at a pressure $p = 133$ Pa involving the measurements of (i) N₂(B) and N₂(C) fluorescences for a discharge current $I = 40$ mA and a pulse duration $\tau = 200$ μ s and 10 ms, together with (ii) the absolute concentration of NO(X) for $I = 40$ and 80 mA with τ varying from 1 to 4 ms. The results of the model agree reasonably well with the measurements of N₂(B) and N₂(C) decays. It is shown that under these experimental conditions, N₂(B) is always populated mainly via the process $N_2(A) + N_2(X, 5 \leq v \leq 14) \rightarrow N_2(B) + N_2(X, v = 0)$, while the relaxation of N₂(C) is dominated by the pooling reaction $N_2(A) + N_2(A) \rightarrow N_2(C) + N_2(X, v = 0)$. An almost constant concentration of NO(X) is experimentally observed until the remote afterglow, but the present model is only capable of predicting the same order of magnitude for afterglow times $t \lesssim 0.05$ s. Several hypotheses are discussed and advanced in order to explain this discrepancy.

1. Introduction

The study of air discharges and their afterglows has been the subject of intense research due to a large number of applications in various domains such as atmospheric chemistry [1, 2], air pollution cleaning [3, 4] and bacterial sterilization by plasma [5]. Accordingly, a considerable number of experimental works concerning discharges or afterglows both in air [6–10] and in N₂–O₂ mixtures [11–16] have appeared in the literature with the purpose of describing the complex kinetics of these media. These works include experiments in coplanar and dielectric barrier discharges [6, 7], corona [13] and nanosecond pulsed discharges at atmospheric pressure [17, 18], as well as low-pressure plasmas, such as dc discharges [10, 11], dc pulsed discharges [8, 9], rf pulsed discharges [14], afterglows of microwave discharges [15] or afterglows produced by dc pulsed discharges [16]. The effect of pressure in air mixtures has been experimentally studied in pulsed discharges [19].

At the same time, theoretical models have been developed with the purpose of simulating these physical systems. The

complexity of nitrogen–oxygen mixtures arises from the coupling between electron and chemical kinetics, due to the important role played by vibrationally excited molecules of the electronic ground state, N₂(X¹ Σ_g^+ , v), the electronic excited state N₂(A³ Σ_u^+) and N(⁴S) atoms, which are strongly correlated with some key species produced in these media, namely O(³P) and NO(X² Π). The understanding of the complex interplay kinetics involving these species is not only important in discharges, but also in the post-discharge regime, where the nitrogen excited states N₂(X¹ Σ_g^+ , v) and N₂(A³ Σ_u^+) constitute the most relevant energetic species. As a matter of fact, the populations of these species can remain significant up to an afterglow time of ~ 10 ms in pure N₂ [20]. Moreover, as pointed out in [12, 16] the study of N₂–O₂ post-discharges can lead to a better knowledge of the elementary processes that occur in these mixtures, such as the relevant reaction channels involving the interaction of N₂(A³ Σ_u^+) with O(³P), O₂(X³ Σ_g^+) and NO(X² Π).

Thus, the formulation of theoretical models for N₂–O₂ discharges or their afterglows should be able to address

these issues and take into account the specific characteristics concerning geometry, source and plasma parameters. Usually, the numerical analysis of the above-mentioned atmospheric pressure discharges takes into account the solutions of a system of particle continuity equations coupled to the Poisson equation, using the local field approximation [21–23]. On the other hand, simulations of low-pressure dc and microwave plasmas involve, in general, steady-state kinetic models based on the coupled solutions to the electron Boltzmann equation and the system of kinetic master equations for the most important heavy species produced in a N_2 – O_2 discharge [24–26] or the time evolution of the several plasma species from the ignition of the discharge until the attainment of the steady state [10].

Under non-stationary conditions at low pressures in air plasmas, coupled time-dependent kinetic models have been employed with the purpose of studying sprite streamer chemistry [1, 27] and in the description of pulsed discharges in air [28]. The former study has shown that a time-dependent kinetic model for the rate balance equations of heavy species, including the coupling between the vibrational and chemical kinetics, presents reliable results for a low-pressure dc pulsed discharge in air. Furthermore, time-dependent kinetic models can also be used to provide detailed information of afterglows if the populations of heavy species are calculated with enough accuracy at the end of the discharge/beginning of the post-discharge. In the case of an air mixture, modelling calculations for the post-pulse regime of a pulsed barrier discharge have been presented in [29], while numerical studies of low-pressure N_2 – O_2 time afterglows created by a dc pulsed discharge with a duration of $50 \mu s$ and by a microwave discharge have been carried out, respectively, in [16] and [30]. Since the afterglow properties are controlled by the active discharge, the results presented and discussed in these two works involve distinct situations. Whereas for pulses with a duration of $\sim 50 \mu s$, the species concentrations are still increasing and the vibrational excitation of N_2 can be neglected, the same does not occur in stationary discharges, where the population of the active species produced in N_2 – O_2 becomes very important, playing in turn a major role in the afterglow kinetics.

An intermediate situation was studied in a recent paper [8], where the experimental investigation of a low-pressure afterglow of a single dc pulsed discharge in air with pulse durations ranging from $200 \mu s$ up to 10 ms was undertaken. Within this time interval, some key species, such as $N_2(X^1 \sum_g^+, v)$, $N_2(A^3 \sum_u^+)$, $N(^4S)$, $O(^3P)$ and $NO(X^2 \Pi)$, are sufficiently populated to play a relevant role in the overall kinetics. Hence, the main purpose of this paper is to present a systematic analysis of the post-discharge measurements performed in [8], by modelling both the pulse and the afterglow regimes. This work follows our previous publication [28], where we have described in detail the heavy-species kinetics of low-pressure dc pulsed discharges in air, considering closely the experimental conditions reported in [8, 31]. Here, we will extend our previous study to the analysis of the afterglow of such pulsed discharges.

The structure of this paper is as follows. In section 2 we report the relevant details of the kinetic model considered for

the pulse and the afterglow. The results of our study, including a comparison between the model predictions and previous measurements concerning the afterglow, are presented and discussed in section 3. Finally, section 4 summarizes the main conclusions of this work.

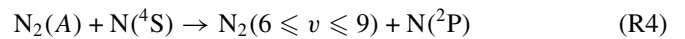
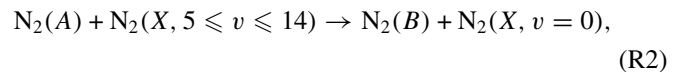
2. Modelling details

The kinetic model used in this paper is composed of two separate modules, one for the dc pulsed discharge and the other for the time afterglow. Basically, our calculations begin with the simulation of the pulsed discharge where the temporal evolution of the concentrations of the neutral and ionic species is determined by taking into account the solutions to the time-dependent system of their rate balance equations. Once these populations are known at the end of the pulse, their relaxation in the afterglow is then analysed by considering the same system of equations.

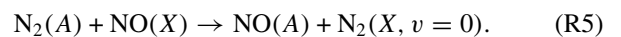
One crucial aspect in this work concerns the connection between these two modules. Since the experimental conditions of this study correspond to a pulse duration range of approximately two orders of magnitude ($200 \mu s$ –10 ms) and owing to the fact that the heavy-particle concentrations obtained at the end of the pulse are introduced as initial values in the afterglow simulations, the correctness of their calculation is of significant importance. The duration of the discharge pulse dramatically influences the role played by relevant processes involving key species, namely $N_2(X, v)$, $N_2(A)$, $NO(X)$, $N(^4S)$ and $O(^3P)$, which lead to different types of behaviour in the plasma and subsequently in the afterglow. For instance, as reported in our previous publication [28] concerning similar discharge conditions, when the pulse duration increases up to 10 ms, the vibrational levels $N_2(X, v)$ become more populated, as well as the concentration of $N(^4S)$ and $O(^3P)$ atoms. Hence, the combined interplay of these kinetics leads to a significant increase in $NO(X)$ via the process



and to a more efficient $N_2(A)$ quenching by $N_2(X, v)$, $O(^3P)$, $N(^4S)$ and $NO(X)$, respectively, through the following reactions:



and



Accordingly, one should expect the metastable $N_2(A)$ to play a major role in the overall kinetics for shorter pulses, while the vibrationally excited $N_2(X, v)$ molecules will be the dominant energetic species for a long pulsed discharge. Therefore, an accurate description of these two species during the pulse is essential in order to obtain reliable sets of initial values to be considered at the beginning of the afterglow.

Moreover, the study of the afterglow should also take into account the coupling of the active species mentioned above, since they constitute the main energy carriers, being precursors for the formation of the main relevant species produced in a N_2 - O_2 mixture. The rate coefficients for reactions (R1)–(R5) have been considered with the following values: (R1), $1 \times 10^{-13} \text{ cm}^3 \text{ s}^{-1}$; (R2), $2 \times 10^{-11} \text{ cm}^3 \text{ s}^{-1}$; (R3), $7 \times 10^{-12} \text{ cm}^3 \text{ s}^{-1}$; (R4), $4 \times 10^{-11} \text{ cm}^3 \text{ s}^{-1}$ and (R5), $6.6 \times 10^{-11} \text{ cm}^3 \text{ s}^{-1}$, as in our previous works [25, 28].

The pulse module is based on the one recently presented in [28] for a dc pulsed discharge in air with a time duration ranging from 10^{-4} to 1 s, where the temporal evolution of the heavy species is described by the corresponding kinetic master equations with a N_2 -20% O_2 mixture at $t = 0$ s, assuming that the values of electron density and electron rate coefficients are the same as in a dc discharge for the same pressure and current. We note that these values are obtained in a self-consistent way [26] with the requirement that under steady-state conditions the total rate of ionization compensates exactly the total rate of electron losses by ambipolar diffusion plus electron-ion recombination. In addition to the vibrational distribution function (VDF) of $N_2(X^1\Sigma_g^+, v)$ molecules, the model considers the most populated N_2 electronic states $N_2(A^3\Sigma_u^+, B^3\Pi_g, B'^3\Sigma_u^-, C^3\Pi_u, a'^1\Sigma_u^-, a^1\Pi_g, w^1\Delta_u)$ and O_2 electronic states $O_2(a^1\Delta_g, b^1\Sigma_g^+)$, together with the ground and excited states of atomic nitrogen $N(^4S, ^2D, ^2P)$, atomic oxygen on the ground state $O(^3P)$, as well as other neutral ($NO(X^2\Pi, A^2\Sigma^+, B^2\Pi)$, $NO_2(X, A)$, O_3) and ionic species ($N_2^+, N_4^+, O_2^+, O^+, NO^+$ and O^-). The set of reactions involving these species and their coefficients is fundamentally the same as reported in [28].

With respect to the afterglow module, we consider essentially the same set of reactions as in the pulse without taking into account the electron impact excitation processes. As a matter of fact, the high-energy tail of the electron energy distribution function in N_2 drops very rapidly at the beginning of the afterglow, reaching a quasi-stationary state after a time of about 10^{-7} – 10^{-6} s [32, 33]. Within this time range, the rate coefficients for electron impact excitation of the $N_2(A^3\Sigma_u^+)$ and $N_2(B^3\Pi_g)$ states decrease both about eight orders of magnitude [34]. Therefore, in spite of the presence of electrons for quite long times, as large as a few milliseconds, in the afterglow [35, 36], the electronic collisions are not considered in the system of master rate balance equations. Owing to the fact that the electron kinetic temperature decreases smoothly along an afterglow either in N_2 [32] or in air [19], this means that the effect of electron-vibration (e-V) collisions is not taken into account in the present model for the early and intermediate instants of the afterglow, where the corresponding electronic rate coefficients can be important [33]. The correctness of this assumption will be confirmed in the discussion presented in section 3.2.

3. Results and discussion

Our calculations were carried out under the experimental conditions reported in [8] concerning the post-discharge of a single dc pulsed plasma in air (N_2 -20% O_2) generated

in a pyrex tube of inner diameter 2.1 cm, operating at a pressure $p = 133$ Pa with a gas flow of 2 sccm and a repetition rate of 0.2 Hz. Under these conditions, two different groups of measurements were considered: (i) the decay of the excited states $N_2(B)$ and $N_2(C)$ after a pulse with a discharge $I = 40$ mA and time duration $\tau = 200 \mu\text{s}$ and 10 ms and (ii) the temporal evolution of $NO(X)$ after pulses with the following characteristics: $I = 40$ mA with $\tau = 2$ and 4 ms; as well as $I = 80$ mA with $\tau = 1$ and 2 ms. Whereas the $N_2(B)$ and $N_2(C)$ fluorescences during the afterglow were monitored using time-resolved emission spectroscopy associated, respectively, with the first and second positive systems of N_2 , $N_2(B^3\Pi_g) \rightarrow N_2(A^3\Sigma_u^+)$ and $N_2(C^3\Pi_u) \rightarrow N_2(B^3\Pi_g)$, the $NO(X)$ absolute concentration was measured using time-resolved tunable diode laser absorption spectroscopy in the infrared region. Readers are referred to [8] for further details. Note that under the described discharge conditions, the renewal of gas between each pulse is ensured.

Since a detailed analysis of the afterglow needs to properly take into account the populations of heavy particles at the end of the plasma, we will start our discussion by presenting relevant results in the pulsed discharge for the purposes of this study. We will then proceed to the afterglow analysis, including the comparison with experiment, with emphasis on the temporal variation of the most important mechanisms that occur in these media.

The gas temperature is an input parameter in our simulations. Here, we have assumed a constant gas temperature during the pulse [37] with values $T_g = 600$ K and 800 K, respectively, for $I = 40$ mA and 80 mA, which are an interpolation of the experimental results reported in [24] for a glow discharge. For these two sets of parameters, the reduced sustaining electric field E/N_g (N_g being the gas number density) was self-consistently determined with the values 10.8×10^{-16} and $11.7 \times 10^{-16} \text{ V cm}^{-2}$. We state that under the assumption of using, in our calculations, values for gas temperature corresponding to the experimental results of a dc plasma, which are larger than those obtained for the pulsed discharges under analysis in the present work, our simulations involved an underestimated value for the gas number density for a given pressure. Therefore, the indicated values for E/N_g may be overestimated, leading eventually to overrated electron impact rate coefficients. However, our previous work [28] has shown that the supposition of a constant gas temperature with a value corresponding to the steady-state conditions allows one to obtain a satisfactory agreement with experiment, namely with $[O(^3P)]$ and $[NO(X)]$, whose kinetics depends directly or indirectly on accurate electronic rate coefficients.

In what concerns the afterglow, it is known that the gas temperature decreases to ~ 300 K in the post-discharge, as observed in [36]. Since the experimental value for this parameter is not available under the working conditions of interest in our study, we have assumed in our calculations $T_g = 300$ K, as in [30]. This hypothesis is realistic in the remote afterglow, but leads to underestimated values for gas temperature at the beginning of the afterglow, affecting some rate coefficients, such as those of V–V and V–T processes,

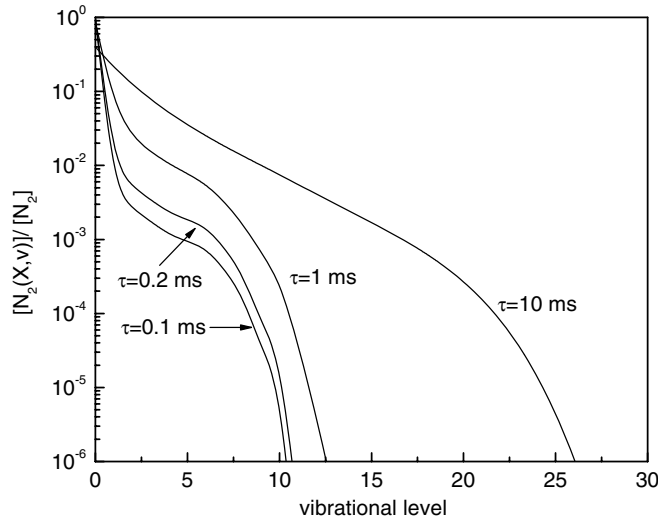


Figure 1. VDFs, $[N_2(X,v)]/[N_2]$, at the end of a pulsed N_2 -20% O_2 discharge for $p = 133$ Pa, $I = 40$ mA and $R = 1.05$ cm with the following durations: 0.1, 0.2, 1 and 10 ms.

together with some chemical rate constants, that depend on T_g . In order to evaluate the effect of this assumption in our simulations, we will analyse the sensitivity of the afterglow module to this parameter in the next section.

Finally, it is worth mentioning that we have used in our calculations $\gamma_N = 1 \times 10^{-4}$ [38] and $\gamma_O = 2.5 \times 10^{-3}$ [39] in the pulsed discharge, while we have considered $\gamma_N = 3.2 \times 10^{-6}$ [40] and $\gamma_O = 2 \times 10^{-4}$ [38] for the afterglow regime.

3.1. Pulsed discharge

Figures 1–4 show the temporal evolution of the concentrations of the vibrational levels $N_2(X, v)$, $O(^3P)$, $NO(X)$, $N(^4S)$, $N_2(A)$, $N_2(B)$ and $N_2(C)$ as a function of the time duration of the dc pulsed discharge in air with $p = 133$ Pa and $I = 40$ mA.

As seen in figure 1, for the higher vibrational levels of $[N_2(X,v)]/[N_2]$, the VDF becomes progressively more populated up to a time duration of 10 ms, which is a result of the combined effect of e-V processes followed by the well-known V-V pumping-up mechanism [34, 41].

Figure 2 reveals that the concentrations of $O(^3P)$ and $NO(X)$ rise monotonically with the pulse duration. In the present calculations, both $[O(^3P)]$ and $[NO(X)]$ increase nearly two orders of magnitude as the pulse duration τ varies from 0.1 up to 10 ms. This behaviour is similar to that reported in [28], where we have compared the concentrations of these two species with experimental results under similar discharge conditions. Here, we just recall that below 10 ms the oxygen atoms are essentially created by the electron impact dissociation of O_2 molecules and through the quenching process $N_2(B) + O_2 \rightarrow N_2(X) + O + O$, while they are lost mainly by the re-association at the wall. As we have stated in [28], the temporal variation of $[NO(X)]$ can be explained through the time-dependent balance between the predominant formation and destruction mechanisms of this species. For $\tau < 5$ ms, the most important populating processes are $N(^2D) + O_2 \rightarrow NO(X) + O$ and $N_2(A) + O \rightarrow NO(X) + N(^2D)$,

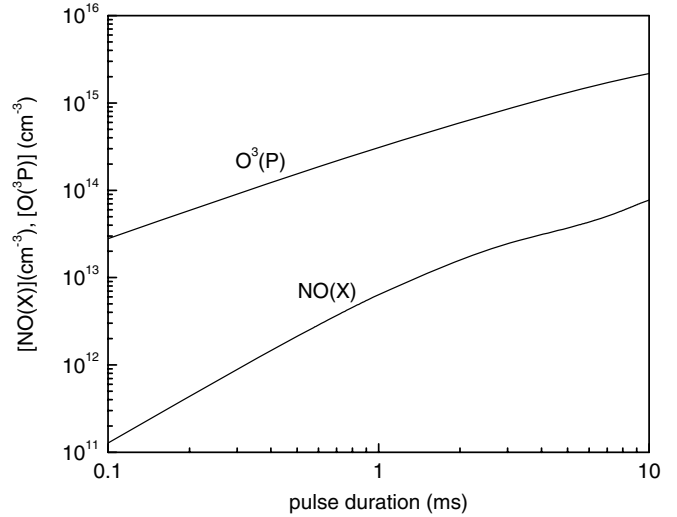


Figure 2. $[O(^3P)]$ and $[NO(X)]$ as a function of the pulse duration of a N_2 -20% O_2 discharge with $p = 133$ Pa, $I = 40$ mA and $R = 1.05$ cm.

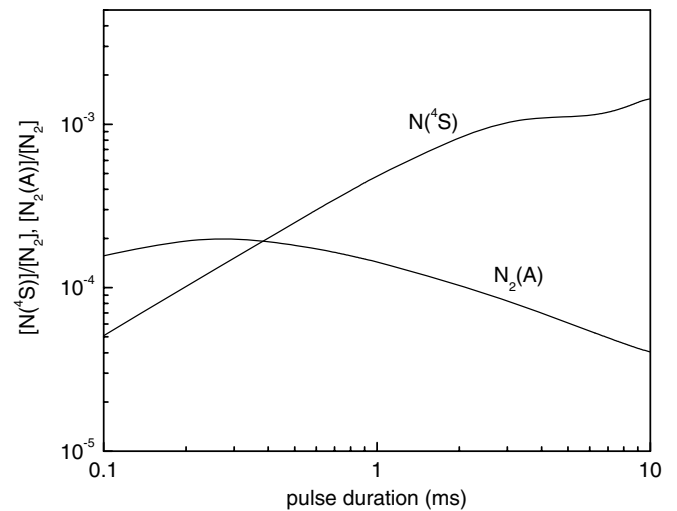


Figure 3. The same as in figure 2, but for $[N(^4S)]/[N_2]$ and $[N_2(A)]/[N_2]$.

while $N_2(X, v \geq 13) + O \rightarrow NO(X) + N(^4S)$ constitutes the most relevant creation channel above this time. Regarding the main $NO(X)$ losses, the main processes are $NO(X) + N(^4S) \rightarrow N_2(X, v \sim 3) + O$ and to a lesser extent, the collision of this species with $N_2(A)$ via reaction (R5). Our present and previous calculations have shown that the balance between these populating and depopulating mechanisms along the pulse results in a significant increase in $[NO(X)]$.

Figure 3 shows that the concentration of nitrogen atoms presents the same trends as $[O(^3P)]$ and $[NO(X)]$, while the population of $N_2(A)$ metastable starts to decrease after $\tau \sim 0.3$ ms. This predicted behaviour for $N(^4S)$ is a result of N_2 dissociation by electron impact collisions, $e + N_2 \rightarrow e + N(^4S) + N(^4S)$ and $e + N_2 \rightarrow e + N(^4S) + N(^2D)$, which constitute the dominating processes in the formation of nitrogen atoms. In parallel, this species is lost mainly via $NO(X) + N(^4S) \rightarrow N_2(X, v \sim 3) + O$, as a consequence of the increase in $[NO(X)]$ with the pulse duration.

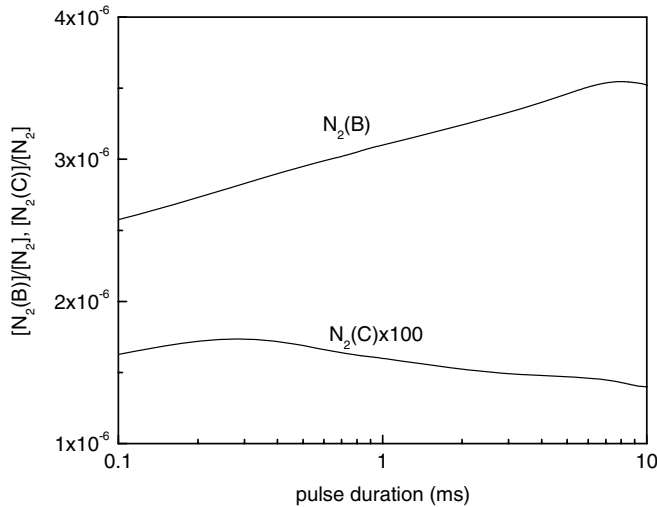


Figure 4. The same as in figure 2, but for $[N_2(B)]/[N_2]$ and $[N_2(C)]/[N_2]$.

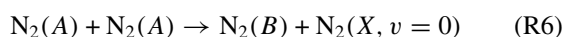
With respect to the diminution of $N_2(A)$, this behaviour is just the consequence of a more efficient quenching by $N_2(X, v)$, $O(^3P)$, $NO(X)$ and $N(^4S)$ via processes (R2)–(R5), since all these species become more populated for longer pulses.

Since we are interested in the analysis of fluorescence emitted from the $N_2(B)$ and $N_2(C)$ excited states in the afterglow, we continue our study by presenting in figure 4 the predicted behaviour for these two excited species along the pulse discharge under the same conditions as those considered in the previous figures. Whereas $[N_2(B)]/[N_2]$ slightly increases with the pulse duration, $[N_2(C)]/[N_2]$ remains almost unchanged along the pulse.

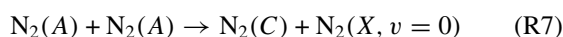
In what concerns $N_2(B)$, this species is essentially created by electron impact, $e + N_2 \rightarrow e + N_2(B)$, as well as from the radiative decays, $N_2(C) \rightarrow N_2(B) + hv$, $N_2(B') \rightarrow N_2(B) + hv$ and $N_2(A) + N_2(X, 5 \leq v \leq 14) \rightarrow N_2(B) + N_2(X, v = 0)$ (R2). These processes contribute, respectively, with $\sim 70\%$, $\sim 13\%$, $\sim 11\%$ and $\sim 3\%$ for the shorter pulse duration of 0.1 ms. As the pulse duration increases, the relevance of the excited vibrational levels becomes more important and consequently the percentage contribution of reaction (R2) to the formation of $N_2(B)$ becomes $\sim 31\%$ for $\tau = 10$ ms, while the contribution of the electron impact process drops to $\sim 50\%$. On the other hand, the loss processes of $N_2(B)$ are, by order of importance, the quenching by O_2 and by N_2 , as well as the radiative decay $N_2(B) \rightarrow N_2(A) + hv$ with relative contributions of $\sim 48\%$, $\sim 36\%$ and $\sim 17\%$, respectively, which are roughly constant during the pulse. Hence, the reported time-dependent behaviour of $N_2(B)$ is the consequence of a more effective production of this species by electron impact and from reaction (R2) with respect to these loss mechanisms.

In our pulse simulations, the temporal evolution of $N_2(C)$ is dominated mainly by electron impact collisions $e + N_2 \rightarrow e + N_2(C)$.

It is worth noting here that the pooling reactions



and



play a minor role in the pulse kinetics of $N_2(B)$ and $N_2(C)$. In fact, the contribution of (R6) to the formation of $N_2(B)$ state is always negligible, while the percentage contribution of (R7) to the production of $N_2(C)$ reduces from $\sim 10\%$ up to 1% as the pulse duration varies from 0.1 up to 10 ms, as a result of the corresponding $[N_2(A)]$ decrease. The rate coefficients for these two processes were taken as follows: (R6), $7.7 \times 10^{-11} \text{ cm}^3 \text{ s}^{-1}$ and (R7), $1.5 \times 10^{-10} \text{ cm}^3 \text{ s}^{-1}$ [25, 28].

Since the afterglow kinetics depends strongly on the pulse duration, let us now point out some of the pertinent results regarding the experimental conditions for the pulse duration τ which were considered in this work, $\tau = 200 \mu\text{s} - 10$ ms:

- (i) the concentrations of $NO(X)$, $N(^4S)$ and $O(^3P)$ will be much larger at the beginning of an afterglow of a pulsed discharge with a time duration of 10 ms;
- (ii) whereas for $\tau = 200 \mu\text{s}$, the fractional concentrations $[N_2(X, v > 5)]/[N_2]$ are smaller than 10^{-3} ; the same does not occur for longer pulses, where these concentrations increase by two or more orders of magnitude;
- (iii) the population of $N_2(A)$ at the end of a pulsed discharge with $\tau = 200 \mu\text{s}$ is about one order of magnitude larger than the one obtained after a pulse of 10 ms.

As we will see in the following, these results will considerably influence the kinetics in the afterglow.

3.2. Afterglow

3.2.1. N_2 excited states kinetics. Figures 5(a) and (b) report the calculated temporal relaxation of the VDF in the afterglow of a pulsed discharge with a duration of $200 \mu\text{s}$ and 10 ms, respectively. These two figures reveal that the VDF remains practically unchanged up to 1 ms after the end of the pulse. However, as the afterglow time increases, the tail of the VDF passes through a maximum at ~ 10 ms, as a result of more efficient V–V collisions. Since the concentrations of the higher vibrational levels become significantly larger when the pulse duration increases, this effect is more pronounced for the longer pulse duration, as shown in figure 5(b). Figures 5(a) and (b) also show that the relative populations of the vibrational levels $N_2(X, v \geq 1)$ are always larger for a pulse duration of 10 ms. Finally, we can also verify that the VDF becomes completely depleted for longer afterglow times.

We will now proceed to the analysis of the nitrogen excited states in the afterglow, by presenting in figure 6 the predicted relative concentrations $[N_2(A)]/[N_2]$. This figure shows that the concentration of this species is always larger in the afterglow of the shorter pulse duration. We should expect this result at the beginning of the afterglow, since it corresponds to the calculated values at the end of the pulse, shown previously in figure 3, where the populations of this metastable state are larger for $\tau = 200 \mu\text{s}$. Furthermore, since the abundance of $N_2(X, 5 \leq v \leq 14)$, $O(^3P)$, $N(^4S)$, and $NO(X)$ is more important for the longer pulse durations, the $N_2(A)$ loss mechanisms (R2)–(R5) involving these species become much more important, leading then to a faster $N_2(A)$ decay in the afterglow of longer pulsed discharges.

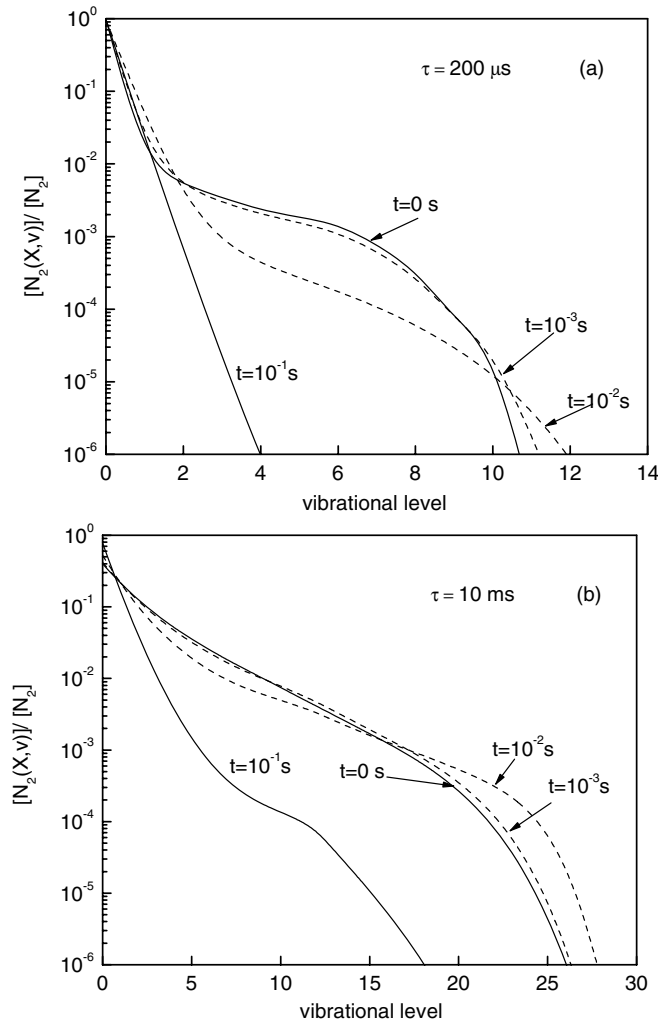


Figure 5. (a) VDF of $[N_2(X,v)]/[N_2]$ molecules in the afterglow of a dc pulsed discharge in air with $p = 133$ Pa, $I = 40$ mA, $R = 1.05$ cm and a pulse duration of $200 \mu\text{s}$ at different afterglow times: 0 , 10^{-3} , 10^{-2} and 10^{-1} s. (b) The same as in (a), but for a pulse duration of 10 ms.

The combined effect of $N_2(A)$ metastable state, together with that of the VDF, is of considerable importance in the interpretation of the observed $N_2(B)$ and $N_2(C)$ fluorescences in the afterglow. Figures 7(a) and (b) represent, respectively, the measured (gray curves) and calculated values (black curves) for the concentrations of $N_2(B)$ along an afterglow of a pulsed discharge in air for a pulse duration of $200 \mu\text{s}$ and 10 ms with pressure $p = 133$ Pa, $I = 40$ mA and $R = 1.05$ cm, while figures 8(a) and (b) report the same information, but for $N_2(C)$. In these figures, the experimental beginning of the afterglow was properly taken into account, as well as the contribution of the background noise. Let us also recall that these experimental results were obtained by time-resolved emission spectroscopy associated, respectively, with the first and second positive N_2 systems assuming that the intensities are proportional to the emitting states. However, since these measurements did not involve a calibration in intensity, the fluorescences are known only in arbitrary units. With the purpose of comparing these experimental results with our model calculations, we have normalized the results for an afterglow time of 2×10^{-5} s.

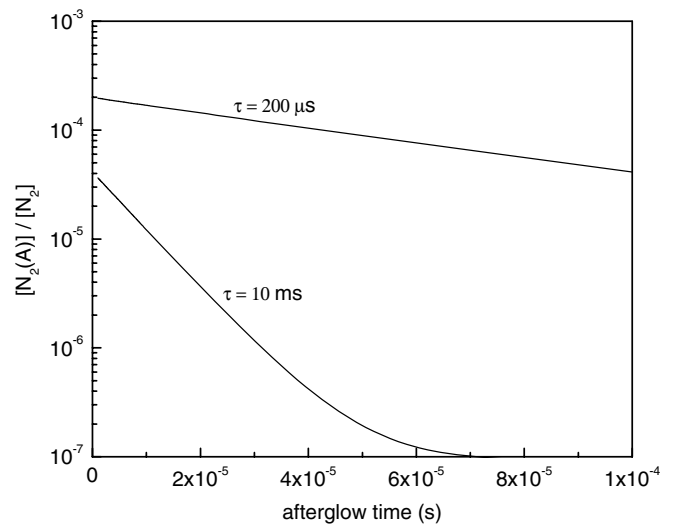


Figure 6. Temporal evolution of the fractional concentration of $[N_2(A)]/[N_2]$ in the afterglow of a dc pulsed discharge in air with $p = 133$ Pa, $I = 40$ mA, $R = 1.05$ cm and a pulse duration of $200 \mu\text{s}$ and 10 ms.

With respect to the $N_2(B)$ state, figures 7(a) and (b) show that there is a very fast decrease in the $N_2(B)$ fluorescence at the beginning of the afterglow, followed by a longer decay for $t \geq 1 \times 10^{-5}$ s. From the comparison of these two figures we can also conclude that the $N_2(B)$ decay is faster for the afterglow of a pulsed discharge with a duration of 10 ms. Since the contribution of electronic impact excitation of $N_2(B)$ during the afterglow is vanishingly small, the main populating mechanisms of this species for both pulse durations of interest in this work are, by order of importance, the processes $N_2(A) + N_2(X, 5 \leq v \leq 14) \rightarrow N_2(B) + N_2(X, v = 0)$ (R2), the radiative decay $N_2(C) \rightarrow N_2(B) + h\nu$ and $N_2(A) + N_2(A) \rightarrow N_2(B) + N_2(X, v = 0)$ (R6). Our calculations show that the relative percentage contribution of process (R2) increases from $\sim 92\%$ up to $\sim 100\%$ in the afterglow when the pulse duration varies from $200 \mu\text{s}$ up to 10 ms. Thus, even for a pulse duration of $200 \mu\text{s}$, the vibrational levels $N_2(X, 5 \leq v \leq 14)$ are sufficiently populated to play a central role in the formation of $N_2(B)$ state. In order to show the influence of gas temperature in these calculations involving the early afterglow, we also present here the results of our simulations when we consider larger values for T_g in the post-discharge of a pulse with a duration of 10 ms. Hence, figure 7(b) also reports the calculated $N_2(B)$ fluorescences when we use $T_g = 400$ K (dashed-dotted curves) and $T_g = 500$ K (dotted curves). We can observe that for a larger value of the gas temperature, the decay of $N_2(B)$ becomes longer, which is a consequence of the behaviour of the VDF in the afterglow with this parameter.

In what concerns the depopulating mechanisms of this excited state, they are similar for $\tau = 200 \mu\text{s}$ and 10 ms, occurring mostly via the quenching processes $N_2(B) + O_2 \rightarrow N_2(X) + O + O$ and $N_2(B) + N_2 \rightarrow N_2(A) + N_2$. Hence, the results exhibited in figures 7(a) and (b) can be explained through the analysis of $N_2(A)$ and $N_2(X, 5 \leq v \leq 14)$ kinetics in the time range 10^{-5} – 10^{-4} s of interest in the study of fluorescences. It is worth remembering at this point that

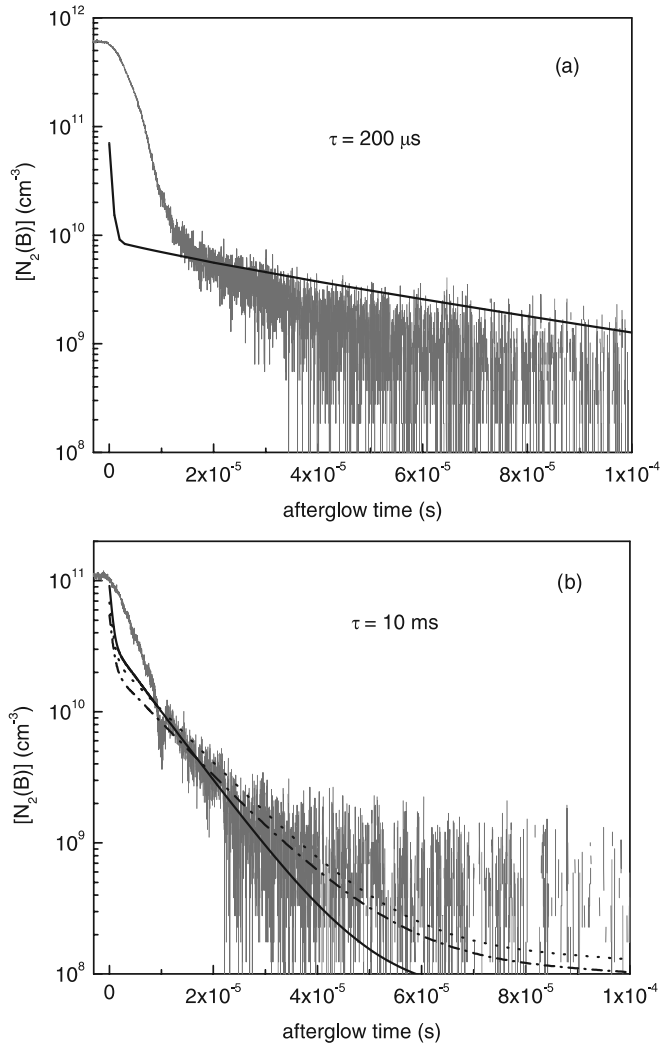


Figure 7. (a) Temporal evolution of the concentration of $N_2(B)$ in the afterglow of a dc pulsed discharge in air with $p = 133$ Pa, $I = 40$ mA, $R = 1.05$ cm and a pulse duration of $200 \mu\text{s}$. The black curves correspond to modelling results, while the gray curves are experimental results presented in [8]. The modelling results are normalized to the experimental ones at $t = 2 \times 10^{-5}$ s. (b) The same as in (a), but for a pulse duration of 10 ms. The full curves correspond to calculations performed with a gas temperature $T_g = 300$ K (reference value), while the dashed-dotted curves and dotted curves were obtained, respectively, for $T_g = 400$ K and 500 K (see text).

in this time interval the VDF remains practically unchanged in the afterglow and becomes more populated for the longer pulse duration, as seen in figures 5(a) and (b). Furthermore, our calculations reveal that in the range mentioned above, $\sum_{v=5}^{14} [N_2(X, v)]/[N_2] \approx 0.0045$ and ≈ 0.124 , respectively, for $\tau = 200 \mu\text{s}$ and $\tau = 10$ ms. In other words, the populations of the relevant vibrational levels for $N_2(B)$ production via process (R2) are larger by a factor of 30 for the longer pulse duration. Hence, one could expect to obtain longer $N_2(B)$ fluorescences in this situation. However, it is important to remember that $[N_2(A)]$ is always larger in the afterglow of the shorter pulse duration, varying from one up to three orders of magnitude within the time range 10^{-5} – 10^{-4} s (see figure 6). Therefore, the joint action of the time variation of

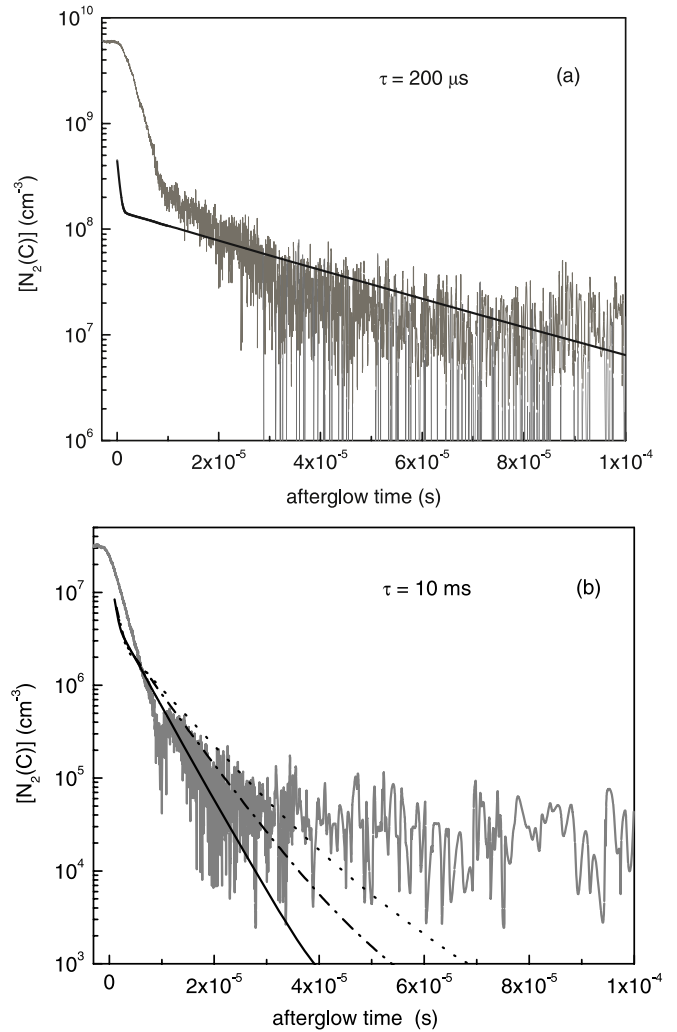


Figure 8. (a) The same as in figure 7(a), but for $N_2(C)$. (b) The same as in figure 7(b), but for $N_2(C)$. The full curves correspond to calculations performed with a gas temperature $T_g = 300$ K (reference value), while the dashed-dotted curves and dotted curves were obtained, respectively, for $T_g = 400$ K and $T_g = 500$ K (see text).

the metastable $N_2(A)$ and the vibrationally excited $N_2(X, v)$ molecules leads to a faster decrease in $N_2(B)$ in an afterglow of a longer pulsed discharge. In spite of the agreement between our calculations and the experimental results for $t \geq 1 \times 10^{-5}$ s, the predictions of our model do not follow the measured shape of the $N_2(B)$ fluorescence for lower afterglow times, which is longer than our results. This discrepancy is mainly a result of the rather large input impedance in the oscilloscope ($5 \text{ k}\Omega$) that was connected to the photomultiplier during the time emission spectroscopy measurements carried out in [8] in order to increase the signal-to-noise ratio for longer afterglow times. As noted by these authors, this procedure, which is a good compromise between the signal-to-noise ratio and the time response of the system, leads to quite long decays at the beginning of the afterglow.

Let us continue our study on the time variation of the fluorescence of N_2 in the afterglow of a discharge with different pulse durations by presenting in figures 8(a) and (b) the experimental and modelling results obtained for $[N_2(C)]$

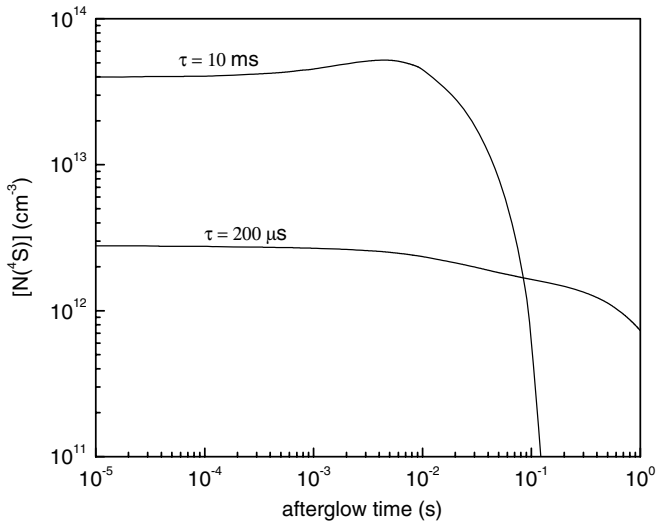


Figure 9. The same as in figure 6, but for $[N(^4S)]$.

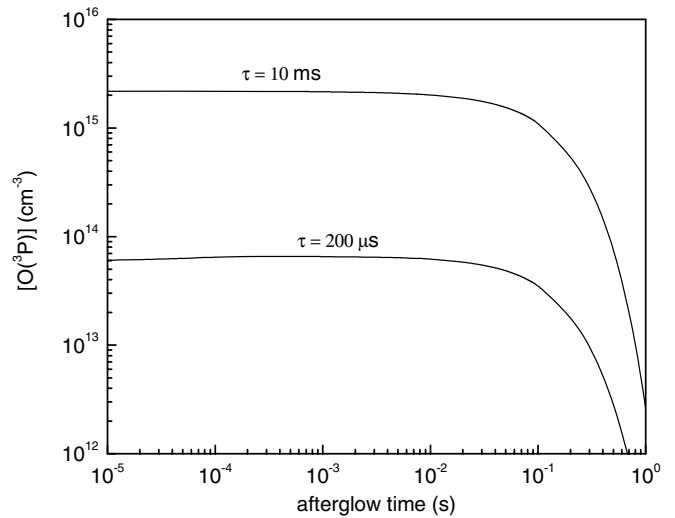


Figure 10. The same as in figure 6, but for $[O(^3P)]$.

under the same experimental conditions as those presented in figures 7(a) and (b). We recall that these results are normalized at an afterglow time of 2×10^{-5} s. We also note that the experimental and the predicted results are represented, respectively, by the gray and black curves. In addition to the discrepancy between the measured and modelling results at the beginning of the afterglow, which has been explained previously, our simulations closely follow the observed $N_2(C)$ fluorescences. The decay of this species can be interpreted from the analysis of its main populating and depopulating mechanisms. Owing to the fact that electron impact processes play a negligible role in the afterglow, the relevant process in an air mixture involving $N_2(C)$ production is the pooling reaction $N_2(A) + N_2(A) \rightarrow N_2(C) + N_2(X, v = 0)$ (R7). Since $N_2(C)$ is essentially depopulated via the radiative decay $N_2(C) \rightarrow N_2(B) + h\nu$, we can conclude that the time variation of $[N_2(C)]$ is ruled by reaction (R7). Figure 8(b) also reports the effect of using larger values for the gas temperature, $T_g = 400$ K (dashed-dotted curves) and $T_g = 500$ K (dotted curves) in the early afterglow of a 10 ms pulsed discharge. This figure shows that the fluorescence of $N_2(C)$ has a longer decay when larger values of T_g are considered in the calculations, as a result of the modification of the temporal relaxation of the VDF. A detailed inspection of figures 8(a) and (b) reveals that the $N_2(C)$ decay is slightly faster for the longer pulse duration, which is a consequence of the temporal variation of the $N_2(A)$ metastable in the afterglow with this discharge parameter.

3.2.2. $N(^4S)$, $O(^3P)$ and $NO(X^2\Pi)$ kinetics. For completeness, figures 9 and 10 report, respectively, the predicted populations of nitrogen and oxygen atoms in the afterglow of a pulsed discharge with $p = 133$ Pa and $I = 40$ mA for the two pulse durations of interest in this work: $\tau = 200 \mu\text{s}$ and $\tau = 10$ ms. These figures show that the populations of these two species are larger when $\tau = 10$ ms, as a result of larger concentrations at the end of the pulse. Moreover, with respect to $N(^4S)$, while the abundance of this species remains nearly constant during the whole afterglow of

pulse duration $\tau = 200 \mu\text{s}$, it decreases abruptly for the longer pulse duration. This behaviour can be explained as follows: in the afterglow of pulse duration $\tau = 200 \mu\text{s}$, the main depopulating mechanism for nitrogen atoms is the process $N_2(A) + N(^4S) \rightarrow N_2(6 \leq v \leq 9) + N(^2P)$ (R4), which is almost compensated by $N(^2P)$ metastable diffusion to the wall, which recycles $N(^4S)$. Concerning the oxygen atoms, the main populating mechanism of this species in the early afterglow is the quenching of metastables $N_2(A, B, a')$ by O_2 , while the dominant depopulating mechanism is the recombination at the wall. This last process is still the most important for $O(^3P)$ destruction after the early afterglow, while the most important populating mechanism of oxygen atoms becomes $NO(X) + N(^4S) \rightarrow N_2(X, v \sim 3) + O$.

For the afterglow of a discharge with a longer pulse duration, that is, $\tau = 10$ ms, the process $NO(X) + N(^4S) \rightarrow N_2(X, v \sim 3) + O$ is also the most important for the production of oxygen atoms, as well as for the destruction of nitrogen atoms during an afterglow with $t < 10^{-2}$ s. In this time range, this process is exactly compensated by the reverse one, $N_2(X, v \geq 13) + O \rightarrow NO(X) + N(^4S)$ (R1), which is clearly dominant in the formation of $N(^4S)$ and in the destruction of $O(^3P)$. However, for longer afterglow times there is a strong depletion of the VDF, leading to a very pronounced decay of $N(^4S)$. This decay then produces a significant decrease in the populating rate of $O(^3P)$ atoms via $NO(X) + N(^4S) \rightarrow N_2(X, v \sim 3) + O$, which also explains the rapid decrease in oxygen atoms at $t \gtrsim 10^{-1}$ s. Finally, we note that in the remote afterglow both these atoms are lost mainly by recombination at the wall.

For the purposes of this work, let us now consider the time dependence of $NO(X)$ during the afterglow of a pulsed discharge in air at $p = 133$ Pa, $R = 1.05$ cm at a low repetition rate (1 Hz) and a gas flow of 100 sccm, where the conditions of discharge current and pulse duration are as follows: $I = 40$ mA with $\tau = 2$ and 4 ms and $I = 80$ mA with $\tau = 1$ and 2 ms, which correspond to the same experimental parameters considered in [8] for the measurements of this species. We

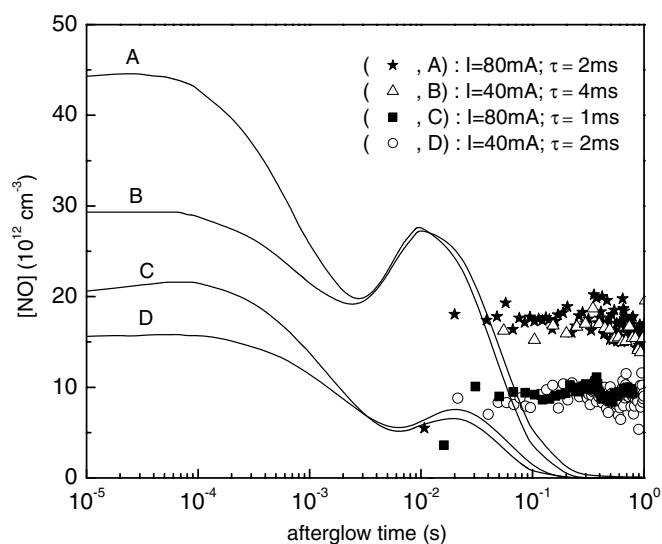


Figure 11. Time variation of $[\text{NO}(X)]$ in the afterglow of a dc pulsed discharge in air with $p = 133$ Pa and $R = 1.05$ cm with the following notation: $I = 80$ mA and $\tau = 2$ ms (\star , curve A); $I = 40$ mA and $\tau = 4$ ms (\triangle , curve B); $I = 80$ mA and $\tau = 1$ ms (\blacksquare , curve C); $I = 40$ mA and $\tau = 2$ ms (\circ , curve D). The symbols are the experimental results presented previously in [8], while the curves correspond to the model predictions.

recall that these measurements were carried out using time-resolved spectroscopy in the infrared region, which permits one to obtain the temporal variation of absolute values of the concentration of $\text{NO}(X)$ along the afterglow.

Figure 11 shows the measured and calculated concentrations of $\text{NO}(X)$ during an afterglow of a pulsed discharge in air with the following notation: $I = 80$ mA and $\tau = 2$ ms (\star , curve A); $I = 40$ mA and $\tau = 4$ ms (\triangle , curve B); $I = 80$ mA and $\tau = 1$ ms (\blacksquare , curve C) and $I = 40$ mA and $\tau = 2$ ms (\circ , curve D), where the symbols correspond to the experimental results, while the curves represent the model predictions. In spite of the qualitative agreement on the order of magnitude of $[\text{NO}(X)]$ for afterglow times ranging from 10^{-2} up to 10^{-1} s, our model fails to describe the experimental results for times beyond this value. Whereas the experimental values of this species remain practically constant for afterglow times $t \geq 10^{-2}$ s, our simulations predict a significant decrease in $\text{NO}(X)$. Since the process $\text{N}_2(X, v \geq 13) + \text{O} \rightarrow \text{NO}(X) + \text{N}(\text{D})$ (R1) plays the central role in $\text{NO}(X)$ kinetics, the results of our model are a consequence of the strong depletion of the higher vibrational levels of the VDF in the time interval 10^{-2} – 10^{-1} s of the afterglow of a pulsed discharge with $\tau = 1$ – 4 ms, which is similar to the behaviour shown in figures 5(a) and (b) for shorter ($200 \mu\text{s}$) and longer (10 ms) pulse durations. We have also analysed the effect of assuming larger values for the gas temperature in the results for the populations of $\text{NO}(X)$. Although not presented in a figure, our calculations have shown that for up to an afterglow time of ~ 1 ms, where the assumption of $T_g = 300$ K may be questionable, we obtain exactly the same general shape for the temporal variation of $[\text{NO}(X)]$. The absolute concentration of this species is slightly smaller when larger values (400 and 500 K) are considered for the gas temperature.

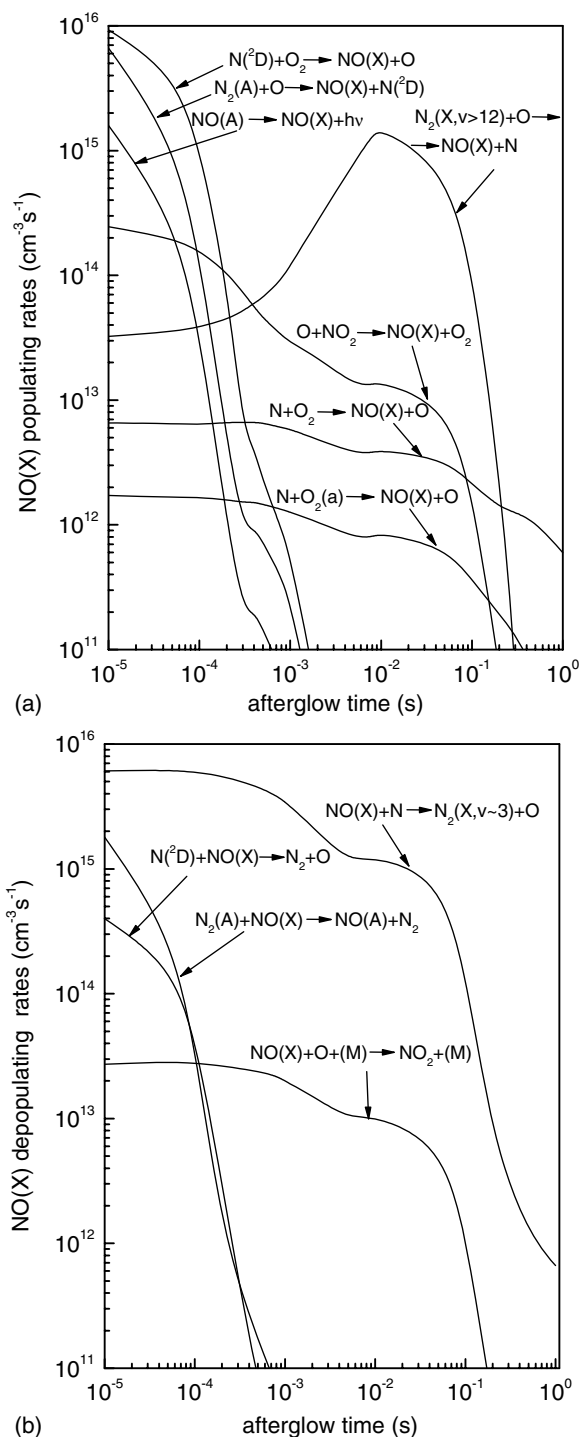


Figure 12. (a) Temporal evolution of the rates of the most relevant populating mechanisms of $\text{NO}(X)$ in the afterglow of a pulsed discharge with $p = 133$ Pa, $I = 40$ mA and $\tau = 2$ ms. (b) The same as in (a), but for the depopulating mechanisms of $\text{NO}(X)$.

Figures 12(a) and (b) represent the temporal variation of the rates of the main populating and depopulating mechanisms of $\text{NO}(X)$ in the afterglow of a pulsed discharge with $p = 133$ Pa, $I = 40$ mA and $\tau = 2$ ms. From the analysis of figure 12(a), we can see that in the early afterglow, $\text{NO}(X)$ is produced by radiative decay, $\text{NO}(A) \rightarrow \text{NO}(X) + h\nu$, as well as by processes $\text{N}_2(A) + \text{O} \rightarrow \text{NO}(X) + \text{N}(\text{D})$ and $\text{N}(\text{D}) + \text{O}_2 \rightarrow \text{NO}(X) + \text{O}$, whose rates decrease by about

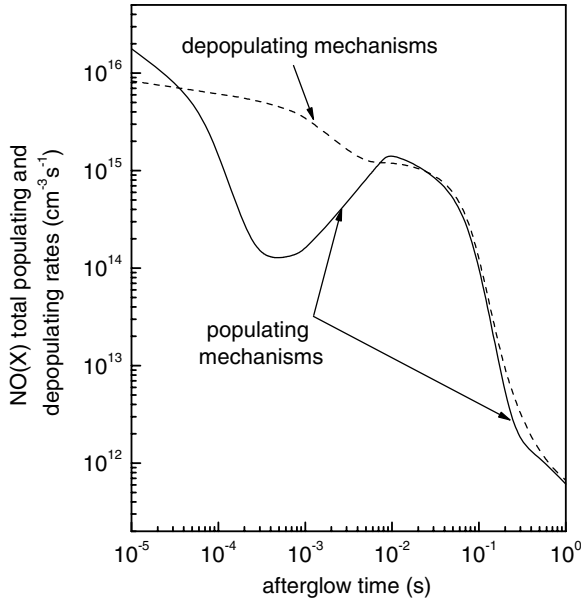


Figure 13. Temporal evolution of the total rate of populating (full curves) and total depopulating (dashed curves) mechanisms of $\text{NO}(X)$ under the same conditions as those of figure 12(a).

four orders of magnitude for $t < 10^{-3}$ s. As the afterglow time increases, process (R1) becomes the most important in populating $\text{NO}(X)$; this result is more pronounced at $t \sim 10^{-2}$ s, as a consequence of a more efficient V-V pumping-up effect, discussed previously in this paper. However, this effect falls abruptly for an afterglow time $\gtrsim 10^{-1}$ s, where the main mechanism responsible for $\text{NO}(X)$ creation involves the collisions of nitrogen atoms with oxygen molecules via the process $\text{N} + \text{O}_2 \rightarrow \text{NO}(X) + \text{O}$. With respect to $\text{NO}(X)$ depopulating processes, figure 12(b) reveals that this species is always destroyed mainly through the reaction $\text{NO}(X) + \text{N}(^4\text{S}) \rightarrow \text{N}_2(X, v \sim 3) + \text{O}$.

It is instructive to continue this analysis by showing in figure 13 the total rate of both populating and depopulating mechanisms of $\text{NO}(X)$ for the case described in the previous paragraph, since it allows enlightening, in more detail, the temporal variation of $\text{NO}(X)$ predicted by the present model. This figure shows several important features: (i) as a result of the joint effect of the sharp decay of the most important creation mechanisms for $\text{NO}(X)$ in the early afterglow ($t < 10^{-4}$ s) and the behaviour of (R1), which follows the VDF in the afterglow, we can observe that up to $t \lesssim 10^{-2}$ s the depopulating mechanisms have, in general, a total rate larger than the populating ones, leading then to the smooth decrease in $[\text{NO}(X)]$ below this afterglow time; (ii) for $t \sim 10^{-2}$ s, the total populating rates are more important than the depopulating ones during a short time interval, where we can observe a slight increase in $[\text{NO}(X)]$ and (iii) finally, for $t \gtrsim 5 \times 10^{-2}$ s, the total depopulating rates become more efficient, which explain the significant decrease in the abundance of $\text{NO}(X)$ in the remote afterglow. Hence, in spite of the relatively small gap between the total populating and depopulating $\text{NO}(X)$ mechanisms for the longer afterglow times (for instance, at $t = 10^{-1}$ s, the total populating and depopulating of $\text{NO}(X)$ rates are, respectively, $1.29 \times 10^{14} \text{ cm}^{-3} \text{ s}^{-1}$ and $1.61 \times 10^{14} \text{ cm}^{-3} \text{ s}^{-1}$), they do not

exactly compensate each other in order to obtain an almost constant $[\text{NO}(X)]$, as observed experimentally. Hence, we can conclude that for $t \gtrsim 5 \times 10^{-2}$ s, the main mechanism for $\text{NO}(X)$ formation, $\text{N} + \text{O}_2 \rightarrow \text{NO}(X) + \text{O}$, is not sufficient to compensate the reaction $\text{NO}(X) + \text{N}(^4\text{S}) \rightarrow \text{N}_2(X, v \sim 3) + \text{O}$, which is always the dominant depopulating mechanism of $\text{NO}(X)$ along the whole afterglow.

3.2.3. Discrepancies between modelling and experiment. From the previous discussion, we can see that the present model is capable of predicting and interpreting the experimental results obtained for $\text{N}_2(B)$ and $\text{N}_2(C)$ fluorescences. Nevertheless, in what concerns $\text{NO}(X)$, in spite of predicting the same order of magnitude as the experimental ones for an afterglow time range 10^{-2} – 10^{-1} s, our model does not describe the measured behaviour for $[\text{NO}(X)]$ in the remote afterglow, where the population of this species remains almost unchanged. This discrepancy may have its origin essentially in the following:

- (i) some missing processes in the present model with an important role in $\text{NO}(X)$ kinetics;
- (ii) an inadequate description of $\text{N}(^4\text{S})$, $\text{O}(^3\text{P})$ and $\text{N}_2(X, v)$, which are the relevant species involving the most important processes responsible for $\text{NO}(X)$ creation and destruction.

With respect to the first point, our model does not take into account several mechanisms responsible for the production of $\text{NO}(X)$, namely

- (a) $\text{N}(^2\text{P}) + \text{O}_2 \rightarrow \text{NO}(X) + \text{O}$ with the rate coefficient $k_a = 2 \times 10^{-12} \text{ cm}^3 \text{ s}^{-1}$ [29];
- (b) $\text{N}(^2\text{D}) + \text{O}_3 \rightarrow \text{NO}(X) + \text{O}_2$ with $k_b = 1 \times 10^{-10} \text{ cm}^3 \text{ s}^{-1}$ [42];
- (c) $\text{N}_2(A) + \text{O}_3 \rightarrow 2\text{NO}(X) + \text{O}$ with $k_c = 4.2 \times 10^{-11} \text{ cm}^3 \text{ s}^{-1}$ [43];
- (d) $\text{N}(^4\text{S}) + \text{O}_2(b) \rightarrow \text{NO}(X) + \text{O}$ with $k_d \sim 10^{-13} \text{ cm}^3 \text{ s}^{-1}$ [44] or $= 2.5 \times 10^{-10} \text{ cm}^3 \text{ s}^{-1}$ [18].

We could expect the process $\text{N}(^2\text{P}) + \text{O}_2 \rightarrow \text{NO}(X) + \text{O}$, indicated in (a), to be relevant under the conditions of this work since its rate coefficient is relatively large in comparison with $\text{N}(^4\text{S}) + \text{O}_2 \rightarrow \text{NO}(X) + \text{O}$, where $k \sim 10^{-17} \text{ cm}^3 \text{ s}^{-1}$ for $T_g = 300 \text{ K}$ [45]. Nevertheless, our calculations show that $[\text{N}(^2\text{P})]$ is always smaller than $[\text{N}(^4\text{S})]$ by more than six orders of magnitude in the far afterglow. A similar argument can be used for the process $\text{N}(^2\text{D}) + \text{O}_3 \rightarrow \text{NO}(X) + \text{O}_2$ mentioned in point (b): in spite of the large rate coefficient of this process the populations of $\text{N}(^2\text{D})$ are always vanishingly small, while those of ozone are about two orders of magnitude smaller than O_2 . With respect to point (c), the process $\text{N}_2(A) + \text{O}_3 \rightarrow 2\text{NO}(X) + \text{O}$ could be a good candidate to provide an extra source of $\text{NO}(X)$ molecules, but as we saw previously (see figure 6), the populations of the $\text{N}_2(A)$ metastable decrease significantly along the afterglow of a pulsed discharge with a longer duration. Finally, concerning $\text{N}(^4\text{S}) + \text{O}_2(b) \rightarrow \text{NO}(X) + \text{O}$, this process has recently been proposed [18] with a rate coefficient of $2.5 \times 10^{-10} \text{ cm}^3 \text{ s}^{-1}$, which is about three orders of magnitude larger than other

values previously reported [44], in order to explain the peaks in NO(*X*) concentration obtained in nanosecond pulsed discharges in air. However, since the concentrations of O₂(*b*) are always much smaller than O₂, it is possible to infer that the process N(⁴S) + O₂(*b*) → NO(*X*) + O would play only a minor role in the NO(*X*) production in comparison with the mechanism N(⁴S) + O₂(*X*) → NO(*X*) + O, which is already considered in the present model.

The observed discrepancy also raises the possibility of having neglected some important phenomena able to fully describe the NO(*X*) kinetics in the remote afterglow. For instance, one of the assumptions of the present model is discarding the electronic impact collisions in the afterglow. As pointed out in section 2, this assumption is certainly true for the production of electronic excited states by direct electron impact, but can be questionable for e-V collisions and stepwise excitation, which have rate coefficients of about the same order of magnitude in the afterglow up to $t < 10^{-3}$ s [33]. For this reason, we have introduced, in the model, the influence of e-V processes in the afterglow, by simply considering the same rate coefficients as those obtained in the pulsed discharge. Concerning NO(*X*) kinetics, the inclusion of e-V collisions could provide, in principle, a better agreement with experiment. As a matter of fact, from the discussion of figures 11–13, it follows that we would obtain a better agreement for the concentration of NO(*X*) in the far afterglow if the role played by the process N₂(*X*, $v \geq 13$) + O → NO(*X*) + N(⁴S) (R1) were more important. Hence, if e-V processes were taken into account, the input of energy into the low vibrational levels would remain for longer times and, accordingly, the population of N₂(*X*, $v \geq 13$) would remain longer as well. As a result of this, the deactivation of the higher vibrational levels of the VDF for $t \gtrsim 10^{-2}$ s would be slower, producing in principle the necessary effect on the concentration of these vibrational levels.

However, in spite of the relatively large values for the e-V rate coefficients, our simulations show that when these processes are considered in the afterglow balance equations, the obtained results for [NO(*X*)] are basically the same. The main reason for this behaviour is the significant decrease in the electron density during the post-discharge, as we show in figure 14 for the case of an afterglow of a pulsed discharge with $p = 133$ Pa, $I = 80$ mA, $\tau = 1$ and 2 ms (full curves, the results for $\tau = 1$ and 2 ms overlap each other) and $I = 40$ mA, $\tau = 2$ and 4 ms (dashed curves, the results corresponding to $\tau = 2$ and 4 ms are almost coincident for the same current).

The electrons in the afterglow are essentially produced by the associative ionization mechanisms, N₂(*A*) + N₂(*a'*) → e + N₄⁺ and N₂(*a'*) + N₂(*a'*) → e + N₄⁺, and they are lost by electron-ion recombination and by ambipolar diffusion to the wall [34] within the time range considered in this figure. It is interesting to mention here that we do not obtain an increase in the electron density at $t \sim 2 \times 10^{-2}$ s, as measured in [35] and interpreted in [34] because the conditions used in that work (afterglow of a microwave discharge) are quite different from those we used here. In particular, we note that the increase in electron density measurements were explained by processes involving collisions with N₂ vibrational levels as

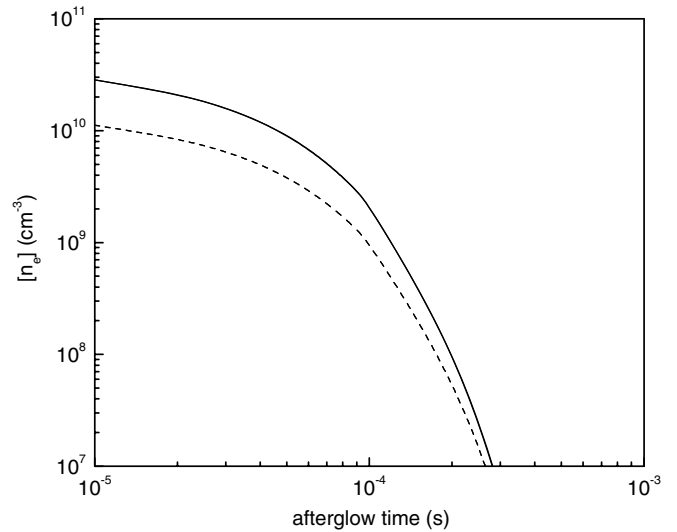


Figure 14. Time variation of the electron density during the afterglow of a pulsed discharge with $p = 133$ Pa, $R = 1.05$ cm, $I = 80$ mA, $\tau = 1$ and 2 ms (full curves) and $I = 40$ mA, $\tau = 2$ and 4 ms (dashed curves). The curves overlap each other for the same current and different pulse durations.

high as $v = 38$ and 39, whose populations are negligible under the conditions of the present work.

In this analysis, we have further checked that the introduction of e-V collisions in the post-discharge description does not produce any modification in the predicted results of other species relevant to this study, which validates one of the main assumptions of our afterglow model.

Taking into account the fundamental processes that influence the VDF in N₂, besides e-V collisions, there is another possible hypothesis involving the wall deactivation of N₂(*X*, v) that could produce a slower decay of the higher vibrational levels in the remote afterglow. As a matter of fact, this mechanism becomes dominant for afterglow times longer than 10^{-2} s, where V-T N₂-N and N₂-O exchanges have a very minor role. Under these conditions, a reduction in the probability γ_v for wall deactivation of N₂(*X*, v) molecules, resulting in principle from some missing surface kinetics, would diminish the depopulating rates of the vibrational levels. In this context, we have tested the effect of decreasing the values of γ_v from 4.5×10^{-4} (reference value [46]) up to three orders of magnitude in our model. The results of these calculations are plotted in figure 15 (dashed curves) for the case of an afterglow of a pulsed discharge with $p = 133$ Pa, $I = 40$ mA and a pulse duration of 2 ms. This figure shows that the NO(*X*) decay is less pronounced in the far remote afterglow when $\gamma_v \sim 4 \times 10^{-6}$. However, to the best of our knowledge, there is no experimental or theoretical study confirming such a significant decrease in the value of this parameter in an afterglow.

Since surface losses depend on many conditions, such as the type of material, morphology, cleanliness, temperature and surface coverage, we can see a large difference between the results presented by different authors [47] in the literature. Hence, although a detailed study of surface kinetics and its influence on the gas phase kinetics is beyond the scope of this

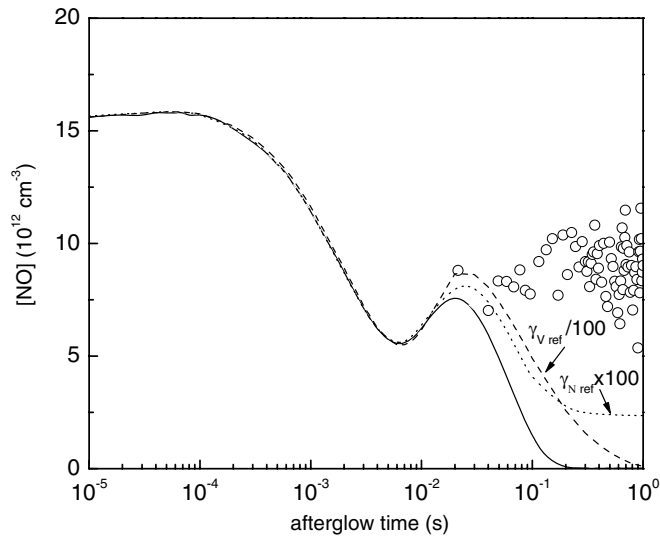


Figure 15. Time variation of $[\text{NO}(X)]$ in the afterglow of a pulsed discharge with $p = 133$ Pa, $R = 1.05$ cm, $I = 40$ mA and $\tau = 2$ ms obtained by the reference model (full curves), when we consider $\gamma_v = 4 \times 10^{-6}$ (dashed curves) and for $\gamma_N = 3.2 \times 10^{-4}$ s (dotted curves). The symbols correspond to experimental values presented in [8].

paper, we have analysed the impact of different surface loss probabilities for $\text{N}(^4\text{S})$ and $\text{O}(^3\text{P})$ atoms in the predicted values of $\text{NO}(X)$ in order to verify whether the observed discrepancies can be attributed to the values of these probabilities. We recall that in the present model, we have used $\gamma_N = 3.2 \times 10^{-6}$ [40] and $\gamma_O = 2 \times 10^{-4}$ [38], respectively, for the probability for wall recombination of nitrogen and oxygen atoms. With respect to γ_N , since the value used for this coefficient is relatively small, we have evaluated the sensitivity of our model when we consider larger values of this parameter. The results of this test are reported in figure 15 (dotted curves) and show that for $\gamma_N \sim 3 \times 10^{-4}$, the predicted values $[\text{NO}(X)]$ approach significantly the experimental ones, but only for $t \gtrsim 0.2$ s, where we can observe a plateau. However, below this afterglow time, the discrepancies still exist, as the general shape of this species remains practically unchanged. The explanation of this important increment in $[\text{NO}(X)]$ with γ_N comes from the fact that the main depopulating mechanism rates of this species, $\text{NO}(X) + \text{N}(^4\text{S}) \rightarrow \text{N}_2(X, v \sim 3) + \text{O}$, become smaller. In what concerns the influence of the value of γ_O on our model predictions, we have verified that the resulting modifications, namely, in $[\text{NO}(X)]$ are always very small.

4. Summary and conclusions

We have carried out a kinetic study of an afterglow of a low-pressure dc pulsed discharge in air. The present study begins with the determination of the time-dependent solutions to the system of rate balance equations for heavy species along the plasma, which provide the concentration for all relevant neutral and charged species at the end of a pulsed discharge in air. These values are subsequently considered as initial conditions in a time-dependent kinetic model in order to calculate the temporal relaxation of the heavy species during the afterglow.

Our calculations have shown that the roles played by $\text{N}_2(X, v)$, $\text{N}(^4\text{S})$, $\text{O}(^3\text{P})$, $\text{NO}(X)$ and $\text{N}_2(A)$ change significantly when the pulse duration varies from $\tau = 200 \mu\text{s}$ up to $\tau = 10$ ms. In fact, $[\text{N}_2(X, v > 0)]$, $[\text{N}(^4\text{S})]$, $[\text{O}(^3\text{P})]$ and $[\text{NO}(X)]$ continuously increase with the pulse duration, while $[\text{N}_2(A)]$ decreases within this pulse duration range, as a consequence of more efficient quenching processes by these species.

This behaviour has, in turn, an important impact on the afterglow results, which can be summarized as follows:

- (i) the well-known V–V pumping-up effect that occurs in the afterglow is more efficient for the longer pulse duration;
- (ii) the VDF is completely depleted in the remote afterglow of a pulsed discharge in air for both pulse durations $\tau = 200 \mu\text{s}$ and $\tau = 10$ ms;
- (iii) $[\text{N}_2(A)]$ is always smaller in the afterglow of a pulse with $\tau = 10$ ms, as a result of more important quenching processes;
- (iv) $\text{N}_2(B)$ decay is faster in the afterglow of the longer pulse, since the most important populating mechanism of this species, $\text{N}_2(A) + \text{N}_2(X, 5 \leq v \leq 14) \rightarrow \text{N}_2(B) + \text{N}_2(X, v = 0)$, is more sensitive to the relatively low population of $\text{N}_2(A)$ metastables when $\tau = 10$ ms than to the temporal relaxation of the VDF;
- (v) $\text{N}_2(C)$ also decays slightly faster in the afterglow of a pulsed discharge with the longer duration. The reason for this comes from the fact that the total populating rate mechanisms for $\text{N}_2(C)$ resulting from the pooling reaction $\text{N}_2(A) + \text{N}_2(A) \rightarrow \text{N}_2(C) + \text{N}_2(X, v = 0)$ become smaller when $\tau = 10$ ms, as a result of the observed behaviour of $\text{N}_2(A)$ in the afterglow mentioned above;
- (vi) $[\text{N}(^4\text{S})]$ and $[\text{O}(^3\text{P})]$ are in general larger during the afterglow of the longer pulse duration, being almost constant up to an afterglow time of ~ 0.1 s. The kinetics of these species is essentially dominated by the strong coupling between the processes $\text{N}_2(X, v \geq 13) + \text{O} \rightarrow \text{NO}(X) + \text{N}(^4\text{S})$ and $\text{NO}(X) + \text{N}(^4\text{S}) \rightarrow \text{N}_2(X, v \sim 3) + \text{O}$; and
- (vii) $[\text{NO}(X)]$ remains nearly constant during the afterglow of a pulsed discharge in air with a pulse duration ranging from 1 to 4 ms. In most of the afterglow, this species is basically created and destroyed by the two processes mentioned in the previous point.

We have compared the predictions of the present model with recent experimental work [8] involving the measurement of $\text{N}_2(B)$ and $\text{N}_2(C)$ fluorescences, as well as the absolute concentration of $\text{NO}(X)$ along the afterglow of a pulsed discharge. In what concerns the decay of these two N_2 excited states, the agreement between modelling results and experiment can be considered satisfactory. As a matter of fact, our simulations supply relevant information concerning the basic elementary mechanisms which are important to explain the experimental decay observed for the $\text{N}_2(B)$ and $\text{N}_2(C)$ excited states during the afterglow of a pulsed discharge in air, as pointed out above. In particular, we have shown that the mechanism $\text{N}_2(A) + \text{N}_2(X, v \geq 20) \rightarrow \text{N}_2(C) + \text{N}_2(X, v = 0)$ is essential to correctly describe the experimental decay of

$N_2(C)$ in the afterglow of a pulsed discharge in air with $\tau = 10$ ms.

With respect to $NO(X)$, the agreement is not so good. The experiment shows that the concentration of this species is practically the same until an afterglow time $t \sim 1$ s, while our calculations predict this behaviour only until $t \lesssim 0.05$ s. Modelling shows that beyond this afterglow time, the main $NO(X)$ depopulating mechanism, $NO(X) + N(^4S) \rightarrow N_2(X, v \sim 3) + O$, is no longer compensated by $N_2(X, v \geq 13) + O \rightarrow NO(X) + N(^4S)$, whose importance decreases significantly in the remote afterglow, as a result of the strong depletion of the VDF. We have checked many hypotheses to clarify the disagreement between calculated and measured values for $[NO(X)]$, although we were not able to find any decisive explanation. It was verified that this disagreement would decrease by assuming some changes in the wall deactivation probability of $N_2(X, v)$ molecules or in the recombination probability of $N(^4S)$, but even then the predictions do not match the experimental results.

Since in our previous work concerning only pulsed discharges in air [28] we have obtained very good agreement between predicted and experimental results for $NO(X)$ measurements, we can conclude that the present model may not take into account certain specific effects that seem to be more relevant in the afterglow regime. In this context, a very promising aspect is the possibility of $NO(X)$ production via surface catalysed recombination, as it has recently been observed in [48] under relatively similar experimental conditions. Therefore, future work will continue both in Porto, Lisboa, and Ecole Polytechnique, Palaiseau, France, in order to include the role of these surface processes in our simulations.

Finally, it is important to mention that the present model may be improved by including the temporal variation of the gas temperature. The consideration of this effect will lead to more accurate values for the rate coefficients associated with V–V and V–T processes, which have a major role in the temporal evolution of the VDF. Moreover, a detailed description of the gas temperature would lead to more precise values for the gas number density not only during the pulse, but also in the afterglow regime. In spite of this limitation, this work provides simulation results that have satisfactory agreement with experiment. Further, it supplies a detailed interpretation of the measurements, including a comprehensive study of the heavy-species kinetics behaviour during the afterglow of pulsed discharges in air with different durations.

Acknowledgments

Part of this work has been developed within the framework of a FCT/CNRS cooperation between Portugal and France.

References

- [1] Gordillo-Vázquez F J 2008 *J. Phys. D: Appl. Phys.* **41** 234016
- [2] Pasko V P 2007 *Plasma Sources Sci. Technol.* **16** S13
- [3] Penetrante B M and Schultheis S E (ed) 1993 *Non-Thermal Plasma Techniques for Pollution Control: Part A—Overview, Fundamentals and Supporting Technologies and Part B—Electron Beam and Electrical Discharge Processing* (Berlin: Springer)
- [4] Penetrante B M, Hsiao M C, Meritt B T, Vogtlin G E and Wallman P H 1995 *IEEE Trans. Plasma Sci.* **23** 679
- [5] Moisan M, Barbeau J, Moreau S, Pelletier J, Tabrizian M, Phillip N and Yahia L H 2001 *Int. J. Pharm.* **226** 1
- [6] Hoder T, Šira M, Kozlov K V and Wagner H-E 2008 *J. Phys. D: Appl. Phys.* **41** 035212
- [7] Kozlov K V, Wagner H-E, Brandenburg R and Michel P 2001 *J. Phys. D: Appl. Phys.* **34** 3164
- [8] Gatilova L V, Allegraud K, Guillon J, Ionikh Y Z, Cartry G, Röpcke J and Rousseau A 2007 *Plasma Sources Sci. Technol.* **16** S107
- [9] Ionikh Y, Meshchanov A V, Röpcke J and Rousseau A 2006 *Chem. Phys.* **322** 411
- [10] Castillo M, Méndez I, Islyaiakin A M, Herrero V J and Tanarro I 2005 *J. Phys. Chem A* **109** 6255
- [11] Nahorny J, Pagnon D, Touzeau M, Vialle M, Gordiets B and Ferreira C M 1996 *J. Phys. D: Appl. Phys.* **28** 738
- [12] De Benedictis S, Dilecce G and Simek M 1997 *J. Phys. D: Appl. Phys.* **30** 2887
- [13] Simek M, Babický V, Clupek M, De Benedictis S, Dilecce G and Sunka P 1998 *J. Phys. D: Appl. Phys.* **31** 2591
- [14] Dilecce G and De Benedictis S 1999 *Plasma Sources Sci. Technol.* **8** 266
- [15] Boudam M K, Saoudi B, Moisan M and Ricard A 2007 *J. Phys. D: Appl. Phys.* **40** 1694
- [16] Cartry G, Magne L and Cernogora G 1999 *J. Phys. D: Appl. Phys.* **32** 1894
- [17] Pai D Z, Stancu G D, Lacoste D A and Laux C O 2009 *Plasma Sources Sci. Technol.* **18** 045030
- [18] Uddi M, Jiang N, Adamovich I V and Lempert W R 2009 *J. Phys. D: Appl. Phys.* **42** 075205
- [19] Robledo-Martinez A, Sobral H and Ruiz-Meza A 2008 *J. Phys. D: Appl. Phys.* **42** 175207
- [20] De Benedictis S, Dilecce G and Simek M 1999 *J. Chem. Phys.* **110** 2947
- [21] Barni R, Esena P and Riccardi C 2005 *J. Appl. Phys.* **97** 073301
- [22] Eliasson B and Kogelschatz U E 1991 *IEEE Trans. Plasma Sci.* **19** 309
- [23] Liu N and Pasko V P 2006 *J. Phys. D: Appl. Phys.* **39** 327
- [24] Gordiets B F, Ferreira C M, Guerra V L, Loureiro J M A H, Nahorny J, Pagnon D, Touzeau M and Vialle M 1995 *IEEE Trans. Plasma Sci.* **23** 750
- [25] Guerra V and Loureiro J 1997 *Plasma Sources Sci. Technol.* **6** 373
- [26] Guerra V and Loureiro J 1999 *Plasma Sources Sci. Technol.* **8** 110
- [27] Sentman D D and Stenbaek-Nielsen H C 2009 *Plasma Sources Sci. Technol.* **18** 034012
- [28] Pintassilgo C D, Guaitella O and Rousseau A 2009 *Plasma Sources Sci. Technol.* **18** 025005
- [29] Herron J T 2001 *Plasma Chem. Plasma Process.* **21** 581
- [30] Pintassilgo C D, Loureiro J and Guerra V 2005 *J. Phys. D: Appl. Phys.* **38** 417
- [31] Guaitella O, Gatilova L and Rousseau A 2005 *Appl. Phys. Lett.* **86** 151502
- [32] Guerra V, Dias F M, Loureiro J, Sá P A, Supiot P, Dupret C and Popov T 2003 *IEEE Trans. Plasma Sci.* **31** 542
- [33] Guerra V, Sá P A and Loureiro J 2001 *Phys. Rev. E* **63** 046404
- [34] Guerra V, Sá P A and Loureiro J 2003 *Plasma Sources Sci. Technol.* **12** S8
- [35] Supiot P, Dessaux O and Goundman P 1995 *J. Phys. D: Appl. Phys.* **28** 1826
- [36] Sadeghi N, Foissac C and Supiot P 2001 *J. Phys. D: Appl. Phys.* **34** 1779
- [37] Welzel S, Gatilova L, Röpcke J and Rousseau A 2007 *Plasma Sources Sci. Technol.* **16** 822
- [38] Kim Y C and Boudart M 1991 *Langmuir* **7** 2999

- [39] Pagnon D, Amorim J, Nahorny J, Touzeau M and Vialle M 1995 *J. Phys. D: Appl. Phys.* **28** 1856
- [40] Yamashita T 1979 *J. Chem. Phys.* **70** 4248
- [41] Sá P A and Loureiro J 1997 *J. Phys. D: Appl. Phys.* **30** 2320
- [42] Herron J T and Green D S 2001 *Plasma Chem. Plasma Process.* **21** 459
- [43] Herron J T 1999 *J. Phys. Chem. Ref. Data* **28** 1453
- [44] Slanger T G and Black G 1979 *J. Chem. Phys.* **70** 3434
- [45] Kossyi I A, Kostinsky A Yu, Matveyev A A and Silakov V P 1992 *Plasma Sources Sci. Technol.* **1** 207
- [46] Black G, Sharpless R L and Slanger T G 1973 *J. Chem. Phys.* **58** 4792
- [47] Kutasi K and Loureiro J 2007 *J. Phys. D: Appl. Phys.* **40** 5612
- [48] Marinov D, Guaitella O, Rousseau A and Ionikh Y 2010 *J. Phys. D: Appl. Phys.* **43** 115203